Optical calibration enhancement algorithm for the implementation of a designed compressive spectral imaging system

Sergio Andrés Urrea Vecino

Thesis submitted in partial fulfillment of the requirements for the degree of Master of Science in

Electronic Engineering

Master thesis in Electronic Engineering

Director:

Ph.D Henry Arguello Fuentes

Codirector:

Ph.D Hans Yecid Garcia Arenas

Universidad Industrial de Santander

Facultad de Ingenierías Fisicomecánicas

Escuela de Ingenierías Eléctrica, Electrónica y de Telecomunicaciones

Bucaramanga

2025

Table Of Contents

List of Figures

Tables List

Summary

Title: Optical calibration enhancement algorithm for the implementation of a designed compressive spectral imaging system.

Author: Sergio Andrés Urrea Vecino.

Keywords: Perturbation methods, Optical computing, Systems modeling, Predictive models, Optical imaging, Adaptive optics, Optical sensors, Optical signal processing, Image reconstruction, Hyperspectral imaging, Mismatch correction.

Abstract: Spectral imaging has diverse applications that surpass the capabilities of RGB images, including quality checks in the food industry, substance detection, and precision agriculture. Traditional spectral imaging methods require a high amount of measurements to capture a spectral image. On the other hand, compressive spectral imaging aims to reduce the required measurements using compressive sensing techniques. Recent work has shown an improvement in the performance of spectral image reconstruction by designing the coding element. Algorithms are commonly used for reconstruction in model-based approaches to surpass the limitation of data. However, the calibration matrix of the implemented system does not perfectly match the designed sensing matrices due to construction non-idealities. To reduce this gap, this research project focuses on enhancing the measurements of the designed spectral imaging system based on reducing the differences between the designed and implemented system to minimize the disparity between simulation and implementation results.

Resumen

Título: Algoritmo de mejora de la calibración óptica para la implementación de un sistema de imágenes espectrales compresivas diseñado.

Autor: Sergio Andrés Urrea Vecino.

Palabras Clave: Métodos de perturbación, Computación óptica, Modelado de sistemas, Modelos predictivos, Imágenes ópticas, Óptica adaptativa, Sensores ópticos, Procesado óptico de señales, Reconstrucción de imágenes, Imágenes hiperespectrales, Corrección de desajustes.

Resumen: Las imágenes espectrales tienen diversas aplicaciones que superan las capacidades de las imágenes RGB, como los controles de calidad en la industria alimentaria, la detección de sustancias y la agricultura de precisión. Los métodos tradicionales de obtención de imágenes espectrales requieren una gran cantidad de mediciones para capturar una imagen espectral. Por otro lado, las imágenes espectrales compresivas pretenden reducir las mediciones necesarias mediante técnicas de detección compresiva. Trabajos recientes han demostrado una mejora del rendimiento de la reconstrucción de imágenes espectrales mediante el diseño del elemento de codificación. Los algoritmos se utilizan habitualmente para la reconstrucción en enfoques basados en modelos para superar la limitación de los datos. Sin embargo, la matriz de calibración del sistema implementado no coincide perfectamente con las matrices de detección diseñadas debido a las no idealidades de construcción. Para reducir esta brecha, este proyecto de investigación se centra en mejorar las mediciones del sistema de imágenes espectrales diseñado basándose en la reducción de las diferencias entre el sistema diseñado y el implementado para minimizar la disparidad entre los resultados de simulación e implementación.

Publications

Conferences

- **Urrea, S.**, Jacome, R., Asif, M. S., Arguello, H., & Garcia, H. (2023). Optical Solutions for Spectral Imaging Inverse Problems with a Shift-Variant System. In Proceedings of the IEEE/CVF International Conference on Computer Vision (pp. 4157-4164).

- Jerez, A., Blanco, G., **Urrea, S.**, Garcia, H., Castillo, S., & Arguello, H. (2023, November). Dual Optical Design for VIS-NIR Classification based on Single Pixel and Diffractive Cameras. In 2023 IEEE Colombian Caribbean Conference (C3) (pp. 1-6). IEEE.

- Gualdrón-Hurtado, R., Jacome, R., **Urrea, S.**, Arguello, H., & Gonzalez, L. (2024). Learning Point Spread Function Invertibility Assessment for Image Deconvolution. 2024 32nd European Signal Processing Conference (EUSIPCO). IEEE, 2024.

- **Urrea, S.**, Gomez, P., Fonseca K., Garcia, H., & Arguello, H. (2024). Mismatch Correction for End-to-End Designed Phase-Encoded-Based Spectral Imaging System. 2024 32nd European Signal Processing Conference (EUSIPCO). IEEE, 2024.

Journals

- Morales-Norato, D., **Urrea, S.**, Garcia, H., Rodriguez-Ferreira, J., Martinez, E., Arguello, H., ... & Rincón, S. (2023). Hyperspectral camera as a compact payload architecture for remote sensing applications. Applied Optics, 62(8), C88-C98.
- **Urrea, S.**, Jacome, R., Asif, M. S., Arguello, H., & Garcia, H. (2024). DoDo: Double DOE Optical System for Multishot Spectral Imaging. IEEE Journal of Selected Topics in Signal Processing.
- Jerez, A., Blanco, G., **Urrea, S.**, Garcia, H., & Arguello, H. (2024). Spectral Classification using a Dual Optical Setup and Deep Neural Networks. Revista UIS Ingenierías

Introduction

Spectral images are three-dimensional data cubes with two spatial (x,y) coordinates and a spectral dimension λ [Garini et al., 2006] and are employed in different areas such as quality checks in the food industry [Fong et al., 2020], biomedical studies [Breitenbom et al., 2017], precision agriculture [Velasco et al., 2016] and substance detection[Kawase et al., 2011]. Usually, these applications cannot be conducted using traditional RGB images due to their poor resolution on the spectrum, achieving only three spectral bands between 400nm and 700nm. In contrast, spectral images can achieve hundreds of bands, over the ultraviolet spectrum (200nm-380nm), visible spectrum (400nm-700nm), or infrared spectrum (780nm-5000nm). Traditional methods to acquire spectral images are based on scanning, either by scanning along space or the spectrum, making them unfeasible for high temporal resolution applications. For this reason, recent efforts have been made to apply compressive sensing theory[Fornasier and Rauhut, 2015, Donoho, 2006, Wu and Arce, 2011, Ramirez et al., 2011, Arguello and Arce, 2010] to reduce the number of measurements required to acquire the information of the spectral cube. By using compressive sensing techniques in spectral imaging, leading to Compressive Spectral Imaging (CSI), many coding elements have been designed, since it has been shown that designed elements improve the quality of the reconstruction. These coding elements include coded apertures, which block certain parts of the incoming light, diffractive elements, which encode the phase in the wave, or a combination of elements [Arguello et al., 2021a]. After acquiring the 2D projections on the sensor, computational algorithms are employed, to recover the underline high-dimensional signal. For this purpose, several approaches of reconstruction algorithms have been proposed such as neural networks, that rely on data to generalize solutions or gradient-based methods, that using the sensing model converge to a solution without relying on data[Bacca et al., 2023]. Recovery algorithms use the sensing matrix to estimate the underline signal but the acquired measurements are projected on the calibration matrix. The calibration process has to be done to ensure the acquisition of the expected response of the system. This calibration matrix describes the implemented optical system after the calibration process, which in most cases is different from the designed sensing matrix in simulation; therefore, recent efforts have been made to add mismatch regularizers to improve the reconstruction quality of the spectral image [Garcia et al., 2023]. Note that the calibration matrix is worse conditioned than the designed sensing matrix in terms of the relationship between the largest eigenvalue and the smallest non-zero eigenvalues. In this path, this work proposes to implement an enhancement algorithm to alleviate the calibration distortion in a designed compressive spectral imaging system to improve the reconstruction image quality.

1. Objectives

General Objective

To implement an enhancement algorithm to alleviate the distortion in the calibration matrix in an optimized spectral imaging system to improve the reconstruction image quality.

Specific Objectives

+ To obtain a differentiable mathematical model of the acquisition process of a designed compressive spectral imaging system using matrix analysis.

+ To implement the designed compressive spectral imaging system and a side information system in the laboratory of the HDSP group.

+ To acquire a dataset consisting of 10 trios of the acquired coded image, reference spectral image, and simulated coded image from the implemented compressive spectral imaging system in the laboratory of the HDSP group.

+ To develop a deep learning-based algorithm for alleviating the calibration distortion in an optimized compressive spectral imaging system.

+ To validate the developed deep learning-based algorithm by reconstructing a spectral datacube using the enhanced measurements and comparing it with the reconstruction of non-enhanced measurements.

2. Background

2.1. Spectral Imaging

Spectral images are high-dimensional signals that depend at the same time on the x,y position and on the spectrum λ [Garini et al., 2006] with applications in different areas such as quality check in the food industry [Fong et al., 2020], visualization of the chemical distribution of certain medicines [Breitenbom et al., 2017], precision agriculture [Velasco et al., 2016] and substance detection[Kawase et al., 2011].

Due to the amount of information in spectral images, it is necessary to acquire a large amount of measurements. Traditionally, for the acquisition of these images scanning systems, such as the push-broom architecture presented in Fig 2.1b, have been used[Wang et al., 2017] but the number of measurements required is proportional to the number of rows, or columns depending of the direction of scanning, of the spectral image, which makes it unfeasible for some scenes with temporal variation. Other examples of scanning architectures are point scanning(Fig 2.1a), where the spectrum is measured for a single (x,y) point at a time, or wavelength scanning(Fig 2.1c), where the full 2D extent of the spatial information is measured for each band at a time. On the other hand, in the state-of-the-art, the use of compressive sensing techniques has been extensively studied to reduce the number of measurements required to obtain a spectral image.

2.2. Compressive Sensing for Spectral Imaging

Due to the amount of information in spectral images, recent efforts apply compressive sensing theory to spectral imaging, giving name to compressive spectral imaging (CSI), to estimate both

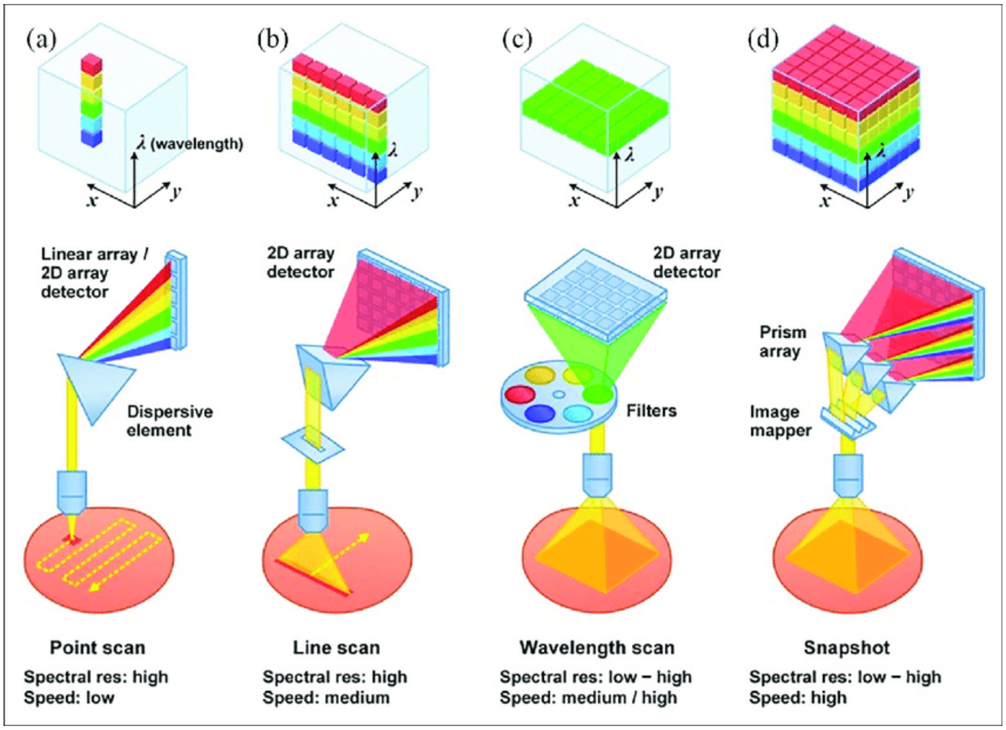

Figure 2.1. Overview of spectral imaging architectures. (Taken from [Wang et al., 2017])

spatial and spectral information solving ill-posed inverse problems. For the implementation of this technique, it is assumed that the system can be modeled as the linear system $\mathbf{y} = \mathbf{H_1}\mathbf{x}$, where $\mathbf{y}$ is the measurement, $\mathbf{x}$ is the spectral scene to be recovered, and $\mathbf{H_1}$ is the sensing matrix representing the system [Yuan et al., 2021]. CSI systems can be divided into two subgroups: first, systems involving amplitude coding, which relies on block-unblock coding, as presented in [Arce et al., 2014], and second, systems that use phase coding, which encodes the phase of the wavefront using different heights and refractive index, to perform this task, as presented in [Marquez et al., 2019].

Amplitude coding has been widely used in the state of the art leading to a variety of CSI systems. There are several proposals such as the Coded Aperture Snapshot Spectral Imager (CASSI) [Garcia et al., 2016], Spatial-Spectral Compressive Spectral Imager (SSCSI)[Salazar et al., 2019], Snapshot Colored Compressive Spectral Imager [Salazar et al., 2019], Dual-Dispersive Coded Aperture Spectral Imager (DD-CASSI)[Monsalve et al., 2021], where the design of sensing matrices using amplitude encoding is made, to recover the underline spectral image.

On the other hand, phase coding elements like diffractive optical elements (DOEs) have been used in optical systems such as the ones presented in [Jeon et al., 2019] and [Peng et al., 2015].

Usually, the inversion problem can not be directly solved, since the acquisition matrix is not square(underdetermined). Therefore, the problem is ill-posed, and gradient-based reconstruction algorithms[Figueiredo et al., 2007], such as gradient-descend, plug-and-play method, are used to solve the inverse problem

$$\hat{\mathbf{x}} = argmin_{\mathbf{x}}||\mathbf{y} - \mathbf{H_1}\mathbf{x}||_2^2 + \tau||\mathbf{x}||_1 \tag{2.1}$$

where τ is a regularization parameter and $||\cdot||_p$ is the L_p norm of a vector. This approach is general in a manner that is not data-driven, thus being suitable for a wide type of scenes. These methods depend directly on the pseudo-inverse of the sensing matrix [Mejia and Arguello, 2018], therefore well-conditioned matrices will result in better reconstruction performance.

2.3. Design of Coding Elements

An important step in improving spectral image reconstruction quality is the design of optimal coding elements, and an optimized matrix $\mathbf{H}_0$. In [Arguello et al., 2023], it is shown that designed coding elements yield better reconstruction quality compared with non-designed coding elements, examples of improvements in reconstruction are shown in Fig.2.2. This improvement is explained by the enhancement in the sensing matrix optimality in terms of condition number, as a result of

Figure 2.2. Multiple optimized, shown at the top, and not optimized, shown at the bottom, coding elements presented on [Arguello et al., 2023], where it is shown that the performance of the optimized coding elements increases compared with not optimized coding elements, where the first two columns show examples of amplitude encoding elements, while the last column shows an example for phase coding elements.

designing the coding elements.

An approach to designing these coding elements is End-To-End (E2E) optimization, which is based on deep learning, using data to learn priors[Arguello et al., 2021b]. E2E models the optical system in a differentiable manner, referring as differentiable to a model where the gradient can be computed, each of the designable elements is designed in a custom layer, and the learnable parameters are the ones that model the coding element. These custom layers are jointly optimized with the reconstruction network.

2.4. Implementation Mismatch in Optimized Coding-Based Architectures

The sensing process of some CSI systems can be modeled as linear, and represented by an impulse response matrix to perform measurements of spectral images. These acquisition matrices rely on ideal linear models that describe the physical phenomena, including operators like convolution with a point spread function (PSF). However, discrepancies can arise between the theoretical model and the implemented optical system due to non-idealities in the material construction or limitations on the alignment and assembly of the system. Consequently, optimization schemes often struggle to reconstruct spectral data from the acquired measurements accurately. The matrix H_0 is the designed sensing matrix, using different optimization strategies such as following the Restricted Isometry Property or following an end-to-end approach. In [Garcia et al., 2023], it was shown that the implemented and calibrated matrix, resulting from the characterization of the implemented system, is worse conditioned, in terms of the condition number than the designed sensing matrix. This analysis is made since the condition number gives an intuition of how the system will react to small changes and it is defined as the division between the largest eigenvalue and the smallest, non-zero, eigenvalue. An example of this is shown in Fig. 2.3.

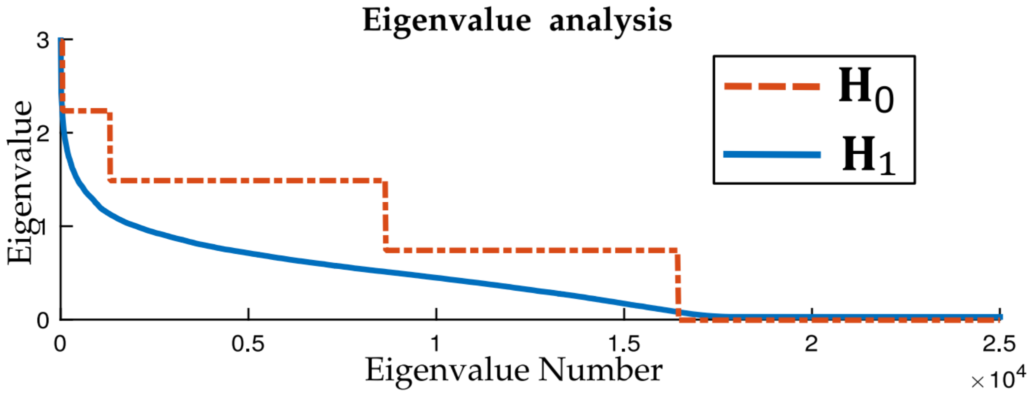

Figure 2.3. Eigenvalues curve comparison between an optimized acquisition matrix $\mathbf{H}_0$, and an implemented optimized acquisition matrix $\mathbf{H}_1$ presented on [Garcia et al., 2023]

3. Sensing Model

To explore the calibration enhancement, it was necessary to model a compressive spectral imaging system, with a differentiable mathematical model to included in the optimization scheme to optimize the encoding element, in the state-of-the-art has been considered multiple types of compressive imaging system including amplitude coding systems, and phase coding systems, in this work, a phase coding based compressive spectral imaging system was employed due to their minimum energy loss compared with amplitude coding [Huang et al., 2022]. Also, it is important to remark that these kinds of systems are very sensible to implementation, and mismatch between the implemented encoding element and the designed encoding element. The compressive spectral imaging system based on phase encoding shown in Fig.3.1 was mathematically modeled as follows, where the equation 3.1 compactly describes the propagation and modulation of the field $u_0(\bar{x}, \bar{y}, \lambda)$ along the optical system:

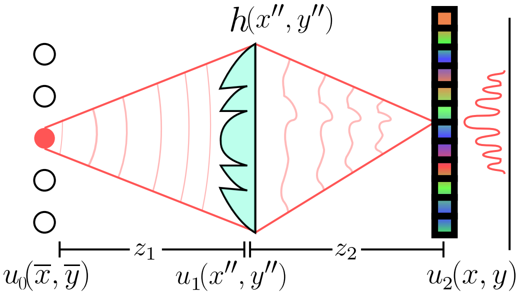

Figure 3.1. Scheme of the compressive spectral imaging system based on phase encoding model.

$$\begin{aligned} G(m,n,c) &\propto \int_{(n)\Delta}^{(n+1)\Delta}\int_{(m)\Delta}^{(m+1)\Delta}\int_{\lambda}\kappa_c(\lambda)|u_2(x,y)|d\lambda dxdy+\varepsilon \\ G(m,n,c) &\propto \int_{(n)\Delta}^{(n+1)\Delta}\int_{(m)\Delta}^{(m+1)\Delta}\int_{\lambda}\kappa_c(\lambda)|\mathscr{P}\{u_0(\bar{x},\bar{y},\lambda)\phi(x'',y'',\lambda),z\}|d\lambda dxdy+\varepsilon \end{aligned} \tag{3.1}$$

Where (x,y) are the spatial dimensions of the sensor, and $u_2(x,y)$ is the encoded wavefront in the sensor, while $G(m,n,c)$ is the discretized and sensed version of the encoded image, λ refers to the wavelength, z represents the propagated distance. (x'',y'') are the coordinates in the encoding element while $u_1(x'',y'')$ is the propagated wavefront in the encoding element as shown in Fig.4.2, and $(\bar{x},\bar{y})$ is the spatial dimensions of the original scene.

Below is the mathematical modeling of each of the wavefront processes along the optical system, such as the propagation model, denoted as the operator $\mathscr{P}$, phase encoding, denoted as the operand $\phi(x'',y'',\lambda)$, and sensing.

3.1. Propagation Model

The wavefront propagation model, considering phase encoding, is described as follows:

$$\mathscr{P}\{u(x,y,\lambda),z\} = \frac{e^{jkz}}{jz\lambda}\iint u(x,y,\lambda)e^{\frac{jk}{2z}((x'-\bar{x})^2+(y'-y)^2)}dxdy. \tag{3.2}$$

The Eq. (3.2) can be rewritten using the convolution operator as

$$\mathscr{P}\{u(x,y,\lambda),z\} = \frac{e^{jkz}}{jz\lambda}\left(u(x,y,\lambda)*e^{\frac{jk}{2z}(x^2+y^2)}\right). \tag{3.3}$$

From the optimization point, the derivative with respect to the input can be defined as:

$$\frac{\partial \mathscr{P}\{u(x,y,\lambda),z\}}{\partial u(x,y,\lambda)} = \frac{e^{jkz}}{jz\lambda}\left(1 * e^{\frac{jk}{2z}(x^2+y^2)}\right) \tag{3.4}$$

3.2. Phase Encoding

Then, the effect of a Phase encoding element, with a height map $h(x'',y'')$ and a diffractive index Δ_{n_λ}, is modeled as $\phi(x'',y'',\lambda) = e^{\frac{j2\pi\Delta_{n_\lambda} h(x'',y'')}{\lambda}}$. Where the height map $h(x'',y'')$ is parametrized using Zernike polynomials as $h(x'',y'') = \sum_{t=1}^{T} Z^t\beta^t$ where Z^t is the t-th Zernike Basis, and β^t the weighting coefficient. It is important to remark that the set of coefficients $\beta = [\beta^1,\beta^2,\beta^3,...,\beta^T]$ will be updated in the optimization scheme. In addition, for optimization purpose, $\frac{\partial\phi(x'',y'',\lambda)}{\partial\beta}$ is defined as:

$$\frac{\partial\phi(x'',y'',\lambda)}{\partial\beta} = \frac{j2\pi\Delta_{n_\lambda}}{\lambda}e^{\frac{j2\pi\Delta_{n_\lambda} h(x'',y'')}{\lambda}}[\frac{\partial h(x'',y'')}{\partial\beta^1},\frac{\partial h(x'',y'')}{\partial\beta^2},...,\frac{\partial h(x'',y'')}{\partial\beta^T}], \tag{3.5}$$

$$\frac{\partial\phi(x'',y'',\lambda)}{\partial\beta} = \frac{j2\pi\Delta_{n_\lambda}}{\lambda}e^{\frac{j2\pi\Delta_{n_\lambda} h(x'',y'')}{\lambda}}[Z^1,Z^2,...,Z^T]$$

3.3. Sensing Model

Finally, the sensing model of the phase-encoded wavefront is modeled as follows:

$$\mathbf{G}(m,n,c) \propto \int_{(n)\Delta}^{(n+1)\Delta}\int_{(m)\Delta}^{(m+1)\Delta}\int_{\lambda}\kappa_c(\lambda)|u_2(x,y,\lambda)|d\lambda dxdy + \varepsilon, \tag{3.6}$$

where $n \in \{0,...,N-1\}$, $m \in \{0,...,M-1\}$ and $\kappa_c(\lambda)$ is the wavelength sensitivity per channel

c of the sensor, and $u_3(x,y,\lambda)$ is the encoded wavefront propagated towards the sensor, while ε represents the gaussian noise of the sensor.

It is important to remark that the derivative of this operator can be computed as:

$$\frac{\partial \mathbf{G}(m,n,c)}{\partial u_2(x,y,\lambda)} \propto \int_{(n)\Delta}^{(n+1)\Delta} \int_{(m)\Delta}^{(m+1)\Delta} \int_{\lambda} \kappa_c(\lambda) sign(u_2(x,y,\lambda)) d\lambda dx dy, \tag{3.7}$$

where $sign(u_2(x,y,\lambda))$ is the sign function, that is not defined in 0, -1 when $u_2(x,y,\lambda) < 0$, and 1 when $u_2(x,y,\lambda) > 0$.

3.4. Linear Operator

Consider a point as the input source such that the PSF of the system can be defined as:

$$\hat{\mathbf{H}}\ (m,n,c) \propto \int_{(n)\Delta}^{(n+1)\Delta} \int_{(m)\Delta}^{(m+1)\Delta} \int_{\lambda} \kappa_c(\lambda) |\mathscr{P}\{\mathscr{P}\{\delta(\bar{x},\bar{y},\lambda),z_1\}\phi(x'',y'',\lambda),z_2\}| d\lambda dx dy + \varepsilon \tag{3.8}$$

Since the system is linear and shift invariant as shown in [Jeon et al., 2019], the convolution with the PSF can also be modeled as a convolution matrix **H** [Vasudevan et al., 2017], this transformation of the operator convolution as a matrix multiplication can be explained by the similarities between the 2D convolution and the matrix multiplication structures, thus the convolution matrix is a Toeplitz version of the convolution kernel, where each row is a shifted copy of the convolution kernel, in this case, the PSF. The acquisition process of a designed compressive spectral imaging system using matrix analysis is defined as follows:

$$\mathbf{y} = \mathbf{H}\mathbf{x} + \varepsilon \tag{3.9}$$

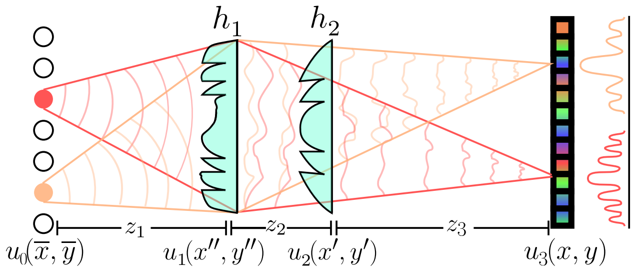

Figure 3.2. System with two diffractive optical elements analyzed.

The derivative of the mathematical model of the acquisition process of a designed compressive spectral imaging system using matrix analysis can be defined as:

$$\frac{d\mathbf{y}}{d\mathbf{x}} = \mathbf{H} \tag{3.10}$$

In the optimization scheme, the forward operator defined on 3.1, was implemented as custom layers in Tensorflow, while the gradient was not defined, since this scheme can be derivated using Tensorflow auto-grad. It is important to remark that the operators used, besides absolute value, are differentiable in all values, while absolute value is not differentiable in 0.

Then it can be concluded that a differentiable mathematical model of the acquisition process of a designed compressive spectral imaging system using matrix analysis was obtained.

3.5. Extension for a Double DOE System

This path explored how to model a system that uses 2 diffractive optical elements besides 1 as shown in Fig.3.2, leading to a system with shift variant properties.

Following the same expressions, the wavefront before the first diffractive optical element can be expressed as:

$$u_1(x'',y'',\lambda) = \mathscr{P}\{u_0(\bar{x},\bar{y},\lambda),z_1\}. \tag{3.11}$$

Then, propagating the encoded wavefront with the effect of the first DOE to the second DOE, a new wavefront is obtained:

$$u_2(x',y',\lambda) = \mathscr{P}\{\phi_1(x'',y'',\lambda)u_1(x'',y'',\lambda),z_2\}. \tag{3.12}$$

The double phase encoded wavefront propagated to the sensor is modeled as:

$$u_3(x,y,\lambda) = \mathscr{P}\{\phi_2(x',y',\lambda)u_2(x',y',\lambda),z_3\} \tag{3.13}$$

Considering $u_3(x,y,\lambda)$ the wavefront that arrives at a high-resolution spatial sensor with $M \times N$ pixels with a pitch of Δ, the discrete measurement in RGB can be defined as

$$\mathbf{G}(m,n,c) \propto \int_{(n)\Delta}^{(n+1)\Delta} \int_{(m)\Delta}^{(m+1)} \int_{\lambda} \kappa_c(\lambda)|u_3(x,y,\lambda)|d\lambda dxdy + \varepsilon, \tag{3.14}$$

where $n \in \{0,...,N-1\}$, $m \in \{0,...,M-1\}$ and $\kappa_c(\lambda)$ is the wavelength sensitivity per channel c of the sensor.

4. Proposed Calibration Enhancement

This proposal is divided into two parts, the first one consists of modeling the mismatches between the design and implementation of a phase-encoded compressive spectral imaging system, by using a proposed degradation model, and the second part consists of using the measurements with the degraded forward model $\bar{\mathscr{F}}_{\beta}\{\mathbf{X}\} = \bar{\mathbf{Y}}$ and the ideal measurements $\mathscr{F}_{\beta}\{\mathbf{X}\} = \mathbf{Y}$, were $\mathscr{F}_{\beta}$ represents the forward model induced by the parameters β introduced in section **3.2**, to solve the following optimization problem:

$$\begin{gathered}\theta = argmin_{\theta} \tau_0 |\mathbf{X} - M_{\phi}\{\mu_{\theta}\{\bar{\mathscr{F}}\{\mathbf{X}\}\}\}|_2^2 + \tau_1 |\mathbf{Y} - \mu_{\theta}\{\bar{\mathbf{Y}}\}|_2^2. \\ \textbf{To Promote} \\ ||\mathscr{F}_{\beta}\{\mathbf{X}\} - \bar{\mathscr{F}}_{\beta}\{\mathbf{X}\}||_2 \geq ||\mathscr{F}_{\beta}\{\mathbf{X}\} - \mu_{\theta}\{\bar{\mathscr{F}}_{\beta}\{\mathbf{X}\}\}||_2\end{gathered} \tag{4.1}$$

Where $\mathbf{X}$ is the input spectral image, $\bar{\mathscr{F}}_{\beta}$ the degraded forward model, $\mathscr{F}_{\beta}$ the ideal forward model, μ_{θ} the proposed projector network, based on a U-net architecture, that reduces the gap between the ideal measurements and the acquired measurements with the degraded model to reduce the mismatch between implementation and simulation, θ the parameters of the projector network, and M_{ϕ} the recovery neural network, based on unrolling network, trained jointly with the ideal forward model $\mathscr{F}_{\beta}$ in an end-to-end optimization scheme solving the optimization problem of equation (4.2), where the heightmap and parameter of the recovery network are optimized with the ARAD1K dataset, before adding the mismatch correction to alleviate the implementation mismatch. It is important to remark that the weights of the recovery network and the height map of the phase encoding element are not fine-tuned during the mismatch correction, while the projector network is learned in this process.

4.1. Proposed Degradation Model

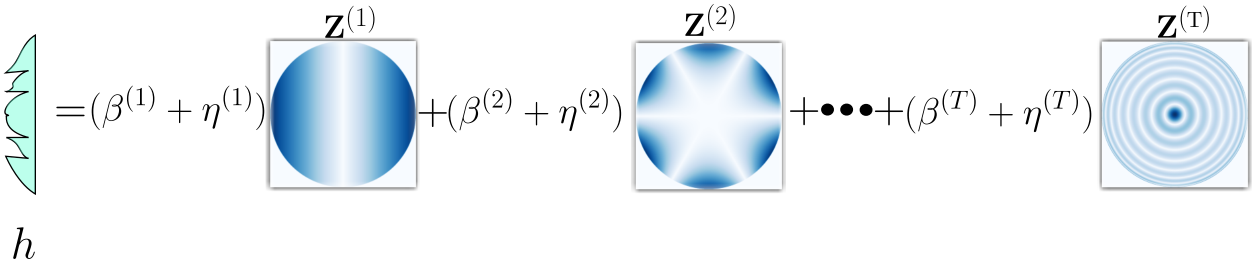

Figure 4.1. Construction of the height map using Zernike polynomials Z, the coefficient set β and the added Gaussian noise η to emulate the possible implementation mismatches.

To model the possible mismatches, it is highly necessary to suit the specifications of the optic elements of the laboratory, and the compressive spectral imaging system is implemented using a deformable mirror DMH40-P01, and due to this element restrictions, the first 15 Zernike bases where used, setting $T = 15$, this work also considers adding Gaussian noise with mean 0 and a standard deviation σ to model the possible mismatches between implementation and simulation, this addition is reasonable since the deformable mirror don't usually have the theoretical zero of the coefficients in the zero of the software thus adding non-expected additional contribution of the basis, rather than affecting the phase in a pixel-wise manner. The manner this noise affects the construction of the height map is shown in Figure 4.1. This work also considers adding Gaussian noise in the sensing step to emulate the noise of the sensor. The effect of this degradation is shown in figure 4.2, and is modeled by $h(x'',y'') = \sum_{t=1}^{T} Z^{t}(\beta^{t}+\eta^{t})$, where η is a sample of a Gaussian distribution with mean 0 and standard deviation σ, also it is important to remark that this degradation, increases the distances between the expected measurement $\mathbf{Y}$ from an ideal forward operator $\mathscr{F}_\beta$ and the acquired measurement $\bar{\mathbf{Y}}$ from the degraded forward operator $\bar{\mathscr{F}}_\beta$.

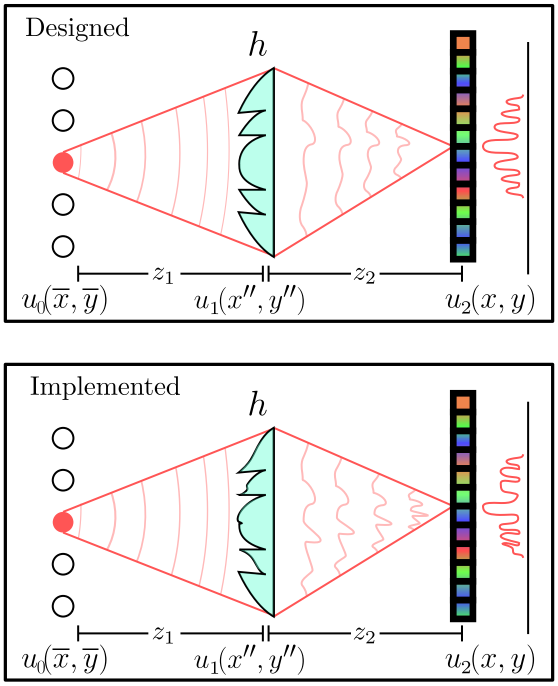

Figure 4.2. Differences between the designed and implemented system and its effect in the sensing.

Also, visual references of the differences in the measurements and height maps between the ideal model $\mathscr{F}_\beta$ and the implemented model $\bar{\mathscr{F}}_\beta$ are shown in figure 4.3.

4.2. Proposed Mismatch Correction

The purpose of this approach is to increase the performance of reconstruction in real scenarios without sacrificing the performance in the optimization step by teaching the network how to behave in real scenarios, such that the projector network, based on a U-net, shown in fig 4.5, composed by 8 convolutional layers and 1 convolution transpose with 2 Relu activations in the mid layers,

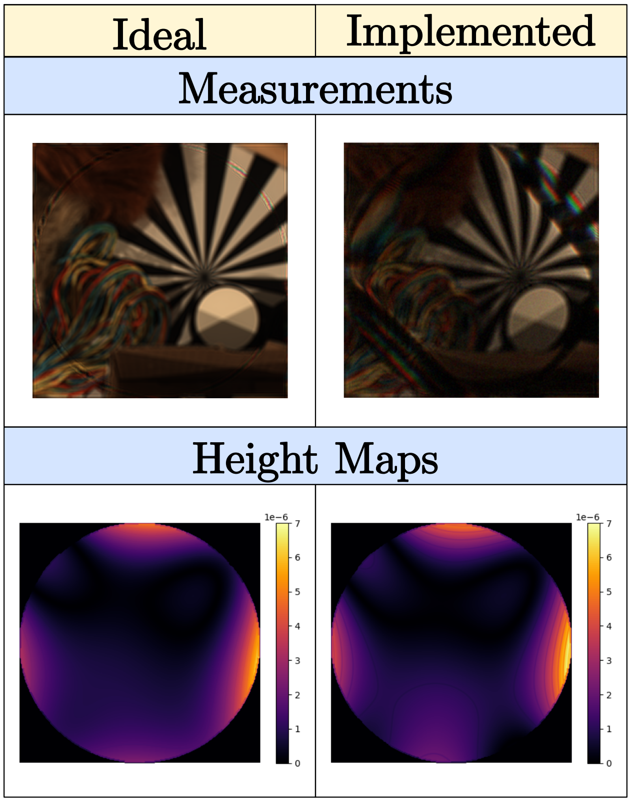

Figure 4.3. Differences between the designed and implemented height maps and their respective measurements.

minimizes the distance between the acquired measurements to the ideal measurements to give better information to the recovery network to achieve better reconstruction results while maintaining the recovery network nontrainable. The proposed projector network was trained using the proposed degradation model, and the ARAD1K dataset, and validated over acquired real images. An overview of the proposed approach is shown in fig 4.4. This work referred to as state-of-the-art (SOTA) using the same trained network as the recovery step, and adding noise to both the sensing and the construction of the height map of the optimized encoding element, to the ideal forward model, emulating the implementation step of the real implementation. This algorithm typically re-

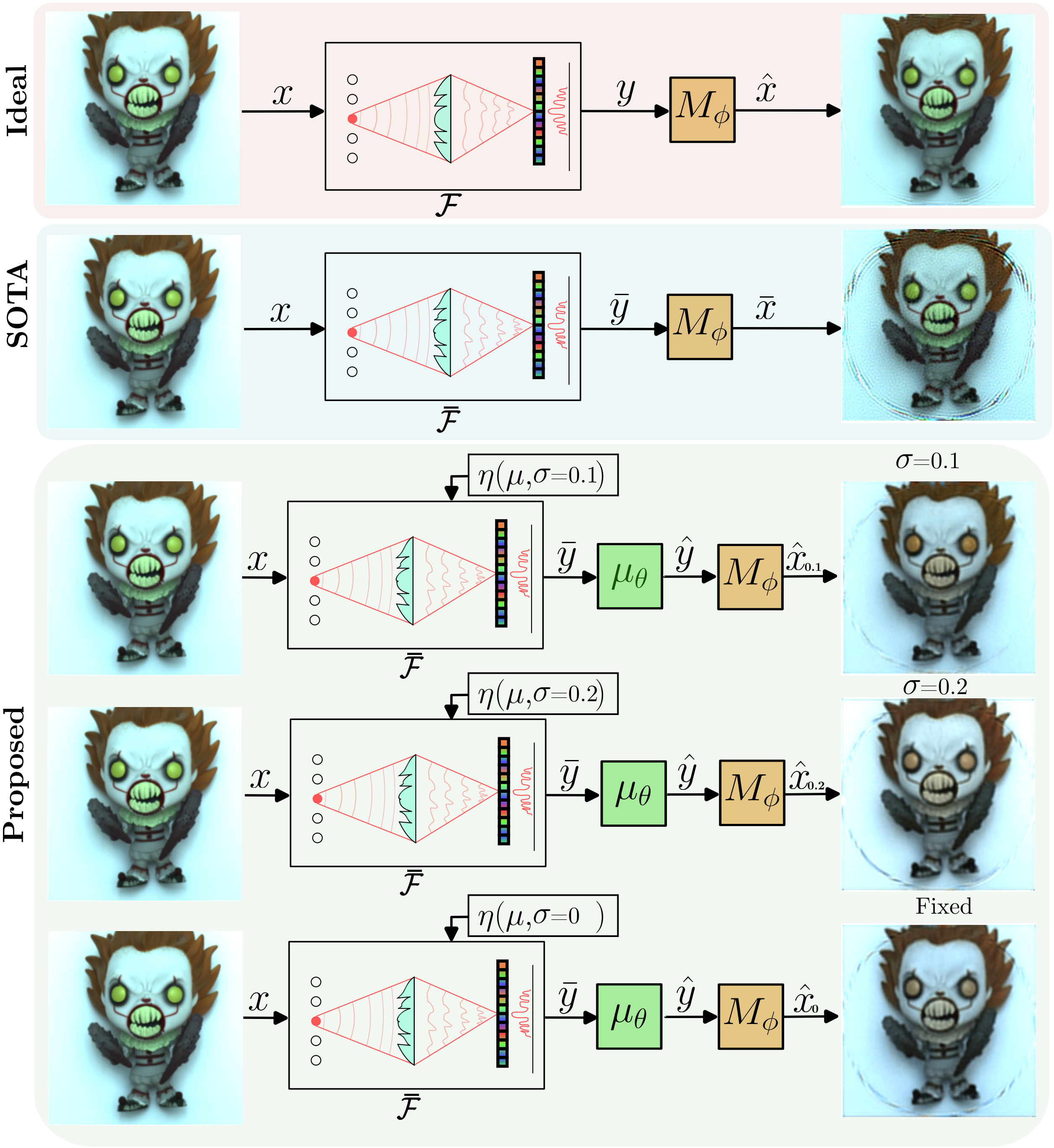

Figure 4.4. Proposed workflow for mismatch correction for a phase-encoded system

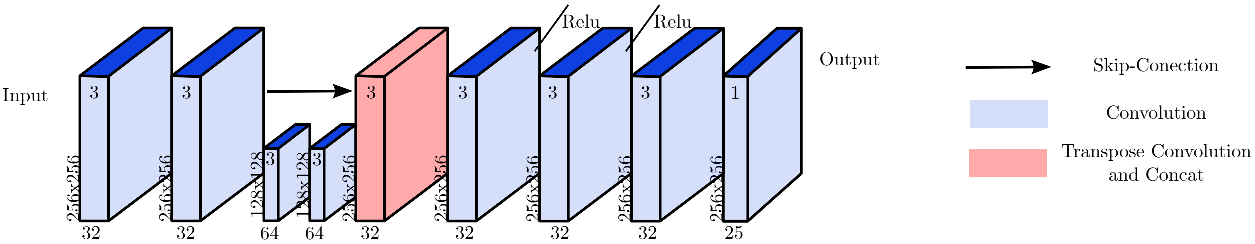

Figure 4.5. Unet architecture used as projector network.

quires a fine-tuning step to improve the implementation results. At the same time, the proposed method does not require the fine-tuning step, since this step also changes the optimized coding element, and requires more data acquisition to be successful. The main restriction to the optimization problem:

$||\mathscr{F}_\beta\{\mathbf{X}\} - \bar{\mathscr{F}}_\beta\{\mathbf{X}\}||_2 \geq ||\mathscr{F}_\beta\{\mathbf{X}\} - \mu_\theta\{\bar{\mathscr{F}}_\beta\{\mathbf{X}\}\}||_2$ is implemented to guide the projector network to the desired measurements even when the distortion is small enough such that $\mathscr{F}_\beta\{\mathbf{X}\} = \bar{\mathscr{F}}_\beta\{\mathbf{X}\}$.

4.3. End To End Optimization

The optimization of both the optical encoder and the recovery network was made using an End-to-End scheme [Arguello et al., 2023], training the set of coefficient β, being restricted to 15 due to implementation restrictions in the Deformable mirror acting as the phase encoding in real life, for the construction of the height map, and the parameters ϕ of the recovery network. Solving the following optimization problem:

$$\phi, \beta = argmin_{\phi,\beta} ||M_\phi\{\mathscr{F}_\beta\{\mathbf{X}\}\} - \mathbf{X}||_2 \tag{4.2}$$

Figure 4.6. Samples of the validation dataset presented in [Arad et al., 2022], used in the optimization process of the end-to-end approach.

Where the neural network is optimized for the designed height map. This optimization is made using the ARAD1K dataset [Arad et al., 2022] composed of 1000 images with dimensions $512 \times 512 \times 31$ scaled to $256 \times 256 \times 25$. The split of the images was 1000 for training, 50 for validation, and 50 for testing. Examples of the validation dataset is shown in figure 4.6. To solve the optimization problem presented in 4.2, the unrolling network presented in [Urrea et al., 2023] named M_ϕ is used. The unrolling network is based on a half quadratic splitting formulation with a prior based on the network proposed on [Gelvez et al., 2021], composed by 7 convolutional layers, with a relu activation after the operation except in the last one where is used a softmax activation, and an adjoint operator based on a U-net type Network, following the same architecture as the one on 4.5. A summary of the network is presented in Figure 4.7, and the optimization was performed using the ADAM optimization of Tensorflow. Also, this Unrolling algorithm can be written as presented in Algorithm 0:

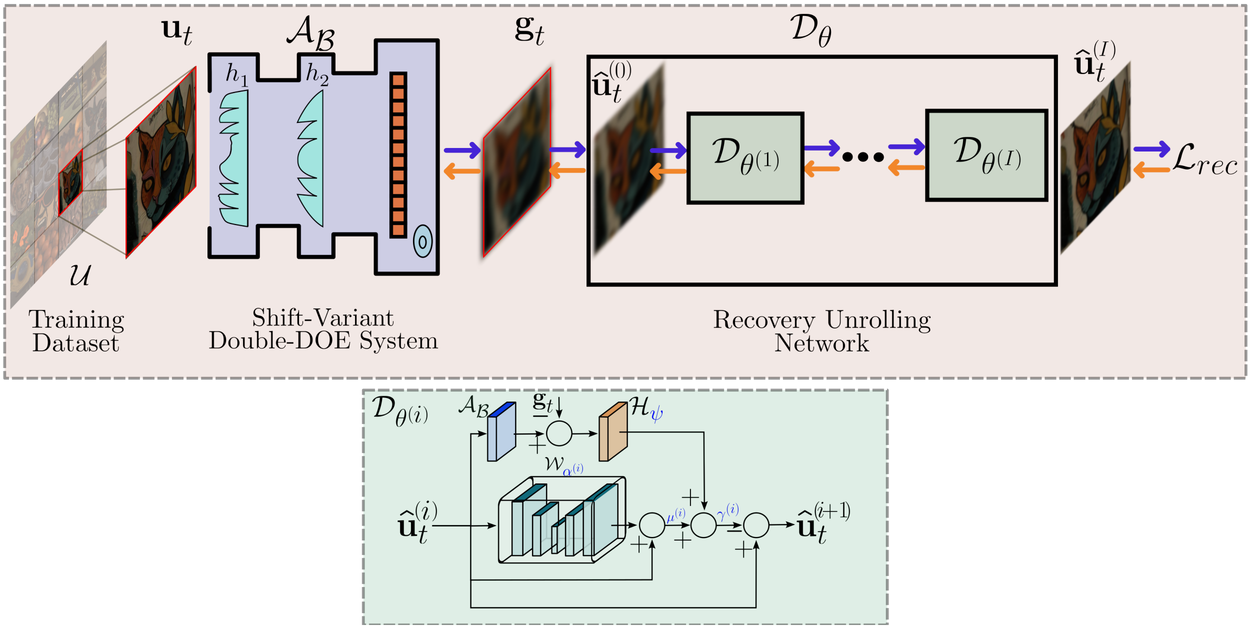

Figure 4.7. Unrolling algorithm and half quadratic splitting adapted from [Urrea et al., 2023]

4.4. Simulations and Results

As mentioned, the simulations are performed over the ARAD1K dataset, the proposed degradation model is tested over 2 Gaussian distributions with mean 0, and σ =0.1 and 0.2, simulation results showed a comparable performance between the proposed method and the ideal simulation, and an improvement when the proposal is compared to the traditional reconstruction.

The mean results for the test dataset are shown in table 4.1, where an increase of performance up to 5 [dB] in terms of PSNR, and 0.06 in SSIM is shown, these results were achieved by

Algorithm 1 Unrolling Algorithm Where $\mathscr{H}_\psi$ is the transpose operator, based on the U-net, following the same architecture as the projector network, $\mathscr{F}_\beta$ the forward operator of the ideal model, $\mathscr{W}_\alpha$ the prior operator based on the mixture-net presented on [Gelvez et al., 2021], and μ, γ weighting coefficients learned in the algorithm.

```
$u^0 \leftarrow \mathscr{H}_\psi\{y\}$
for $i$ in $I$ do
    $a^{i+1} \leftarrow \mathscr{F}_\beta\{u^i\}$
    $b^{i+1} \leftarrow a^{i+1} - y$
    $c^{i+1} \leftarrow \mathscr{H}_\psi\{b^{i+1}\}$
    $d^{i+1} \leftarrow \mathscr{W}_{\alpha^i}\{u^i\} + u^i$
    $e^{i+1} \leftarrow \mu^i d^{i+1} + c^{i+1}$
    $u^{i+1} \leftarrow u^i - \gamma^i e^{i+1}$
end
```

reconstructing the spectral images of the test dataset with an ideal forward model, degraded model, and degraded model with the projector network, using the same recovery network and weights for all the cases. It is important to remark that the proposed method outperforms the state-of-the-art since the corrected measurements are more similar to the ideal measurements.

	Ideal	**SOTA**	$\sigma = 0$	$\sigma = 0{,}1$	$\sigma = 0{,}2$
PSNR ↑	33.90	25.92	30.83	30.71	30.54
SSIM ↑	0.9589	0.8348	0.9052	0.9046	0.9033

Tabla 4.1. Average results of the reconstructed test images in terms of PSNR and SSIM

An illustration of the reconstruction performance is shown in Figure 4.8. Where, it can be observed that the proposed method provides better scene reconstruction, achieving approximately 6 dB improvement in this specific image compared to state-of-the-art methods in the best cases. Notably, the proposed method significantly reduces artifacts and enhances color in the reconstructed hyperspectral images.

In this chapter, a deep learning-based algorithm for alleviating the calibration distortion in

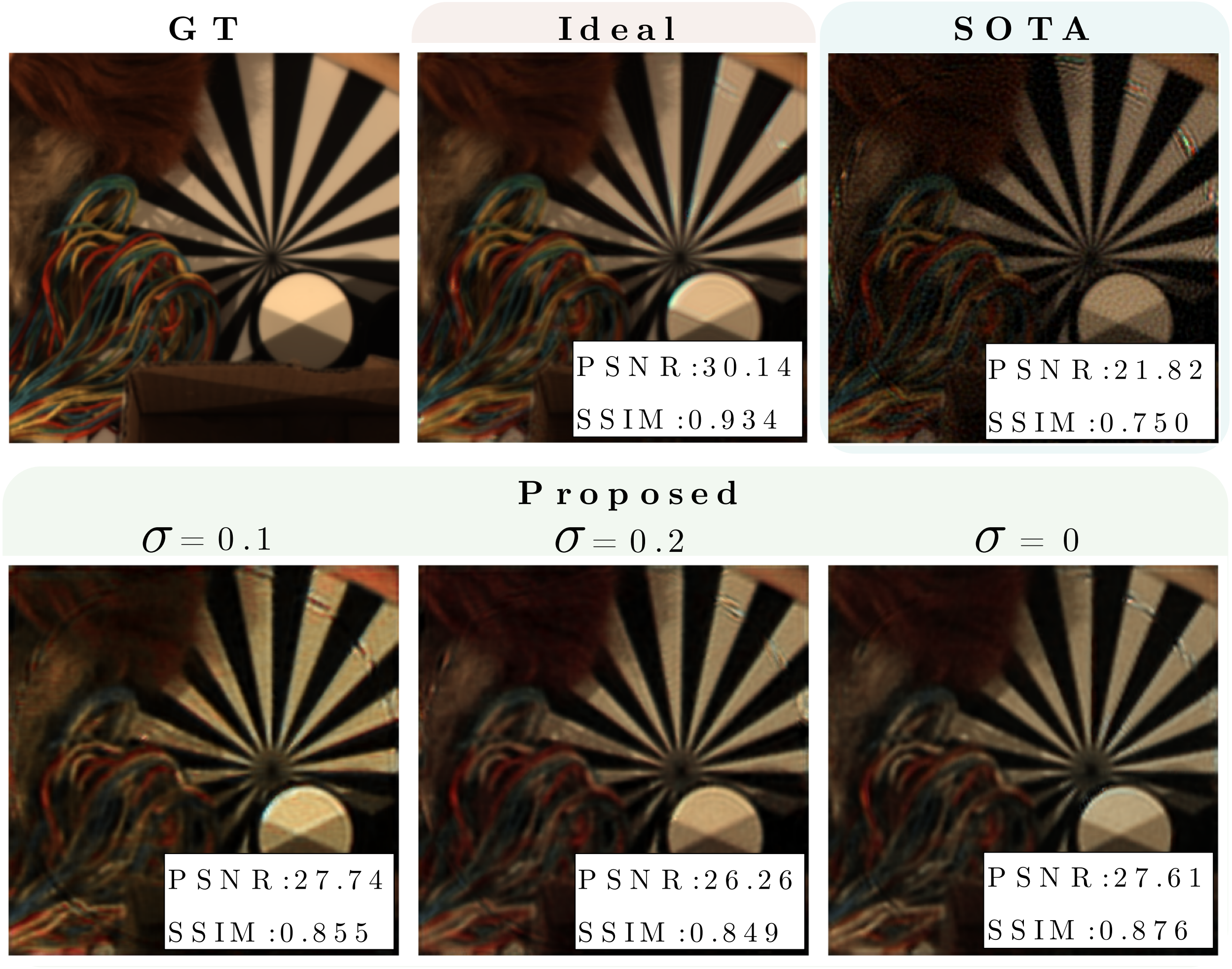

Figure 4.8. Reconstruction results in false RGB for an image in the test dataset of the ARAD1K.

an optimized compressive spectral imaging system, was developed.

5. Validation in Real Scenarios

5.1. Single Phase Encoding System

To evaluate the proposed method for alleviating the mismatch between the simulated and acquired scenes, the compressive spectral imaging system based on phase encoding designed in the end-to-end optimization chapter is implemented that acquires spectral images on the visible range, with side information, as shown in Figure 5.1. The side information system is necessary to validate the reconstruction by comparing the spectral signatures of the recovered and the reference images with and without considering the proposed method by introducing the trained projector network.

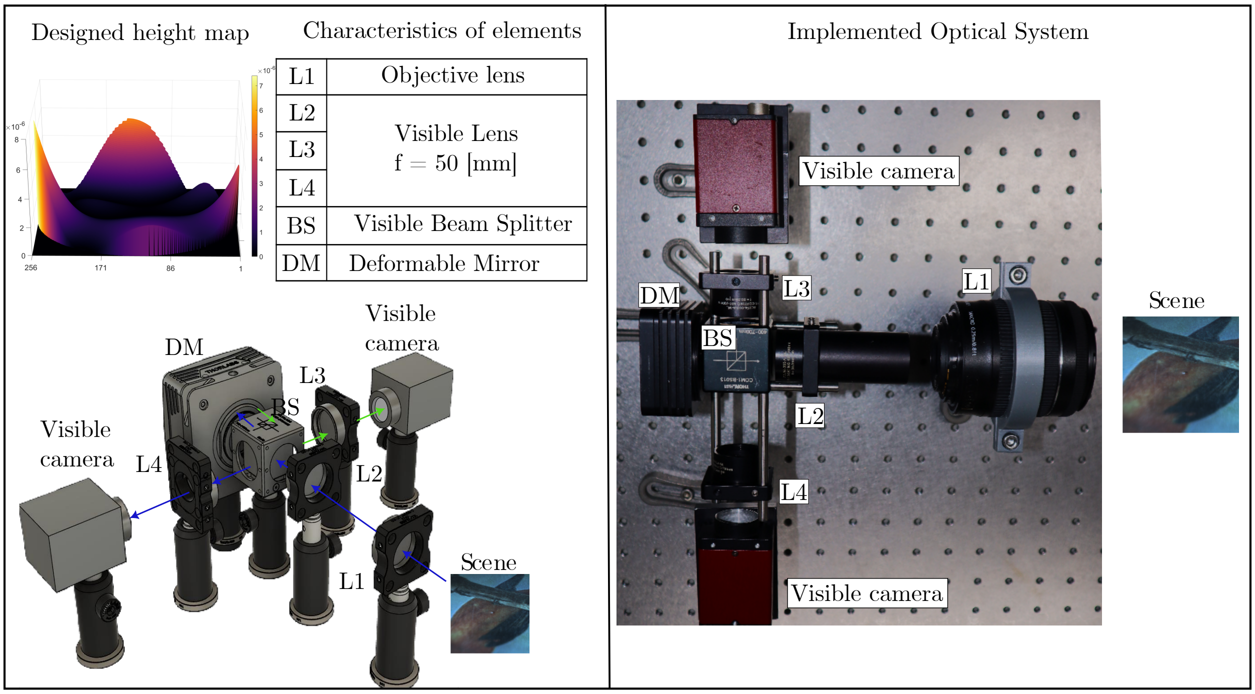

Characteristics of elements

L1	Objective lens
L2	Visible Lens f = 50 [mm]
L3	
L4	
BS	Visible Beam Splitter
DM	Deformable Mirror

Figure 5.1. Optical system for spectral information acquisition with and without wavefront deformation.

The implemented system uses an objective lens (L1) to focus the incident scene light. Then, it implemented two 4F systems, starting with the lens L2 used. From this point, a beam splitter divides the light beam into two. The first path corresponds to the side information stage, which employs a lens L4 to focus the scene on the sensor. The second path corresponds to the transmission path of the beam splitter, where a DMH40-P01 Thorlabs deformable mirror is employed to apply wavefront deformation as phase encoding, acting as the optimized encoding element. Due to implementation limitations, Zernike polynomials from 2 to 14 were used to generate the simulated height map. The distance between lens L2 and the deformable mirror is the Fourier plane. After this modulation, the resulting light beam passes through the same beam splitter and lens L3, focusing the modulated scene on a sensor of the same reference, the used sensor was the stingray F-080B camera, and the lenses L2, L3, and L4 were Ø1"N-BK7. Additionally, it is important to remark that the spectral acquisition of the 25-band scene was performed through band-to-band illumination from 420 to 660 [nm] using a tunable light source. Also spectral reference images were acquired using a wavelength scanning technique with the side information implemented system.

The acquisition of 12 hyperspectral images using the implemented optical system was performed to validate the proposed method's performance. The acquired images from the implemented compressive spectral imaging system are shown in Figure 5.2

The results are shown in Figure 5.3, 5.4, where the GT represents the false RGB representation of the Spectral reference, Acquired the encoded RGB image, and SOTA, $\sigma = 0$, $\sigma = 0{,}1$, and $\sigma = 0{,}2$ the false representation of the reconstructed spectral images, highlight that reconstructions obtained by the proposed method exhibit a better overall structure of the hyperspectral scene, as well as a better color balance compared to state-of-the-art methods.

The Spectral Angle Mapper (SAM) was implemented to compare the reconstructed images, where the smaller number represents a better fitting of the spectral signatures. Mathematically, this metric between to vectors u, and, v is described as:

$$SAM(u,v) = cos^{-1}(\frac{u \cdot v}{|u||v|}) \tag{5.1}$$

were $u \cdot v$ represents the dot product between the vectors, and $| \cdot |$ represents the euclidean norm of the vector.

The spectral angle mapper of the reconstructions of the flower image are presented Table 5.1

	SOTA	$\sigma = 0$	$\sigma = 0{,}1$	$\sigma = 0{,}2$
SAM ↓	0.2614	0.1806	0.0633	0.0995

Tabla 5.1. SAM for the highlighted point of the flower image.

The spectral angle mapper of the reconstructions of the bird image are presented Table 5.2

	SOTA	$\sigma = 0$	$\sigma = 0{,}1$	$\sigma = 0{,}2$
SAM ↓	0.1135	0.1655	0.0787	0.1206

Tabla 5.2. SAM for the highlighted point of the bird image.

On the other hand, the comparison and analysis of a spectral signature of the reconstructed image was conducted, as shown in Figure 5.3, 5.4, highlighting that the proposed method allows to obtain a spectral signature closer to the ground truth, compared to the state of the art.

In addition, the SAM metric of the reconstructed images using the acquired dataset is presented in Table. 5.3, highlighting that the proposed method of correction, with a $sigma = 0{,}1$

achieved the best performance.

	SOTA	$\sigma = 0$	$\sigma = 0{,}1$	$\sigma = 0{,}2$
SAM ↓	0.1304	0.1802	0.1286	0.1403

Tabla 5.3. Mean SAM for the acquired test dataset.

In this chapter, the designed compressive spectral imaging system and a side information system in the laboratory of the HDSP group was implemented, also, a dataset consisting of 12 trios of the acquired coded image, reference spectral image, and simulated coded image from the implemented compressive spectral imaging system in the laboratory of the HDSP group was acquired, finally, the developed deep learning-based algorithm by reconstructing a spectral data cube using the enhanced measurements and comparing it with the reconstruction of non enhanced measurements was validated.

5.2. Double Phase Encoding System for multi-shot spectral imaging

The system presented in Fig. 5.5 was constructed. The Double Phase Encoding system is composed of an objective lens, a beam splitter to acquire spectral references for the neural network fine-tuning, and a deformable mirror as the first encoding, emulating a DOE, then the second encoding, which is a state-of-the-art DOE of [Jeon et al., 2019], known as Spiral, after the encoding, the coded projection is formed over the RGB sensor of a Canon EOS M50, with a pixel size of 3.72μm, as mentioned before, the first DOE is emulated via DMH40-P01 Thorlabs deformable mirror, that adapts the position of each mirror to emulate each learned heightmap.

An image different from the training dataset was acquired and reconstructed, the results are shown in Fig. 5.6. The reconstruction quality employing four shots improves significantly compared to the spiral encoding and by employing fewer shots.

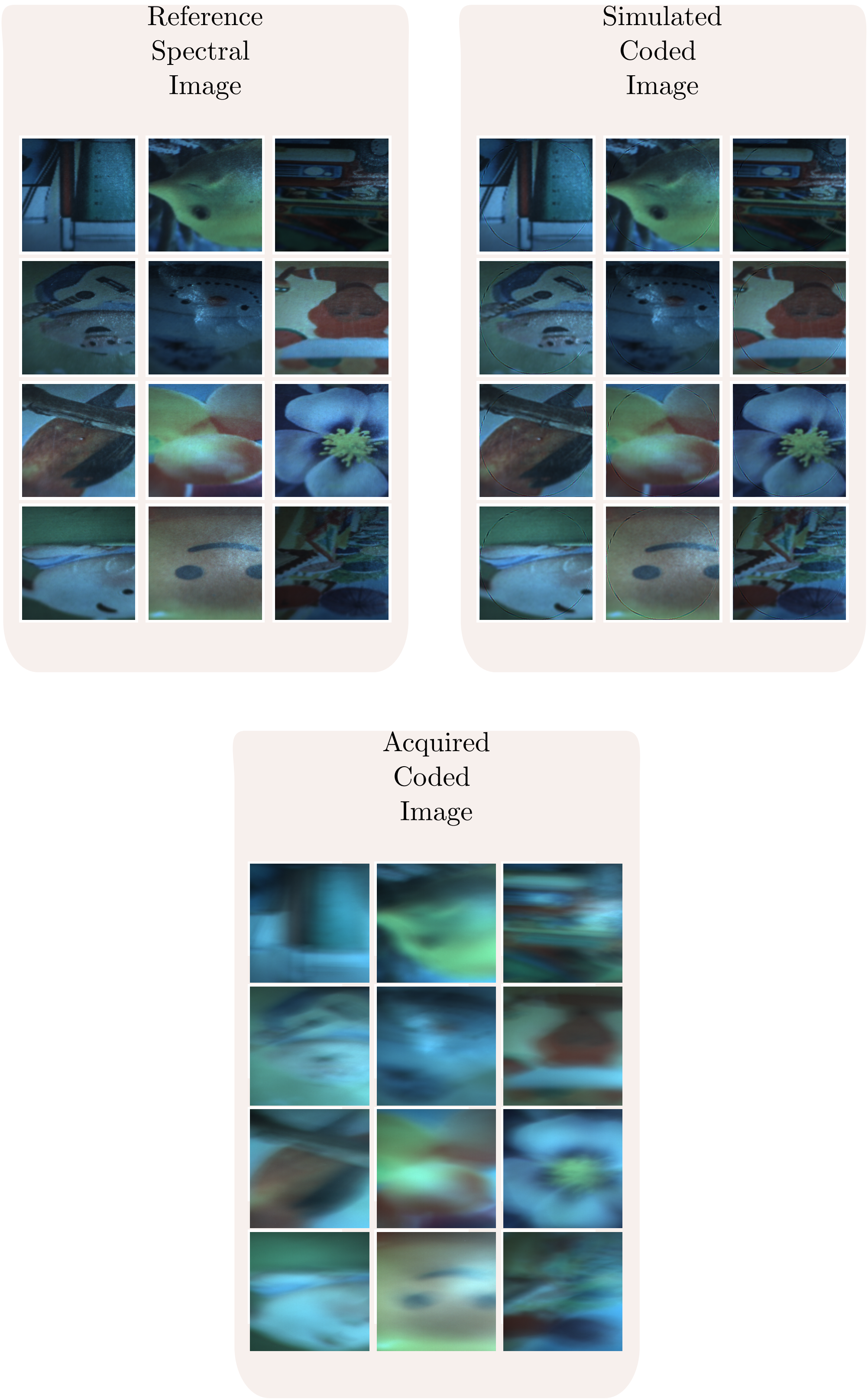

Figure 5.2. False RGB representation of the acquired reference spectral image, acquired coded image, and simulated coded image.

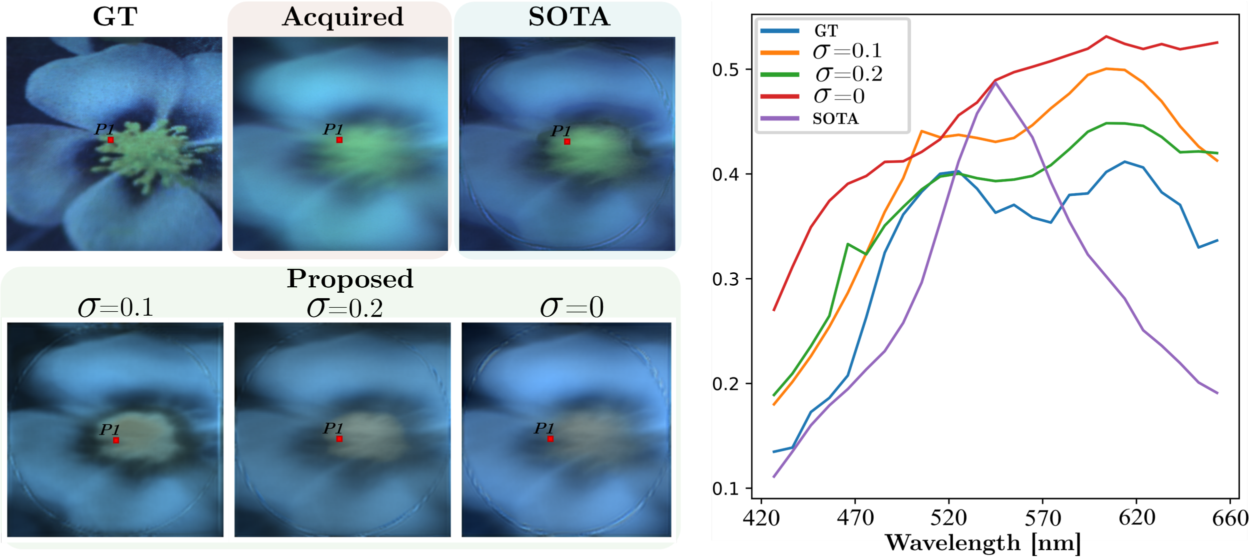

Figure 5.3. Reconstruction results in false RGB for an encoded RGB image acquired with the implemented testbed and spectral signature of specific ROI.

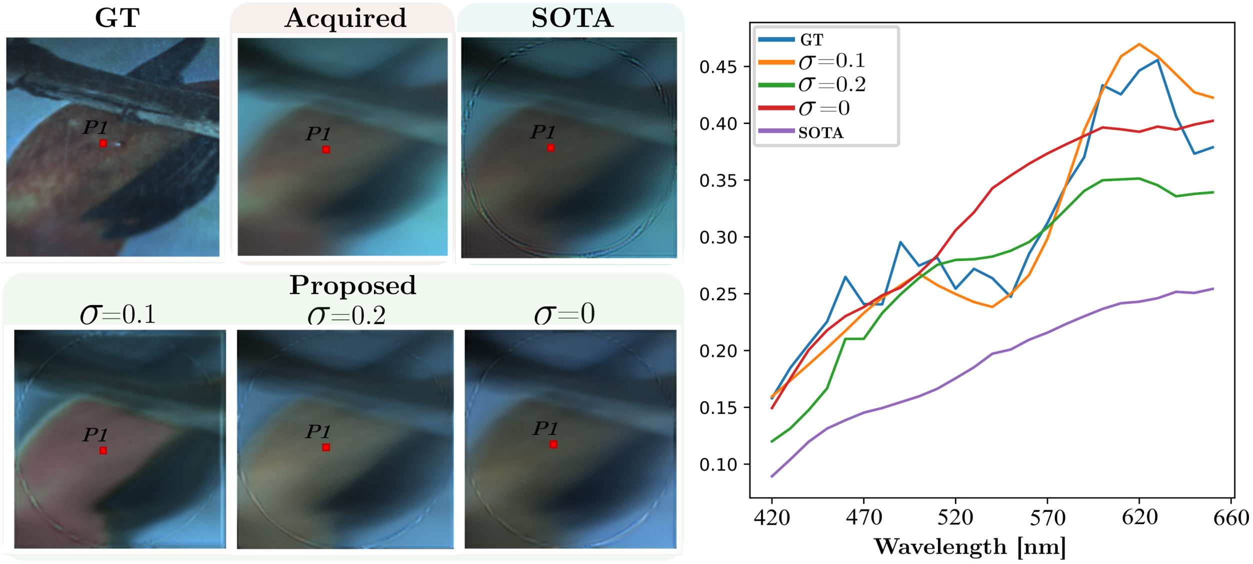

Figure 5.4. Reconstruction results in false RGB for an encoded RGB image acquired with the implemented testbed and spectral signature.

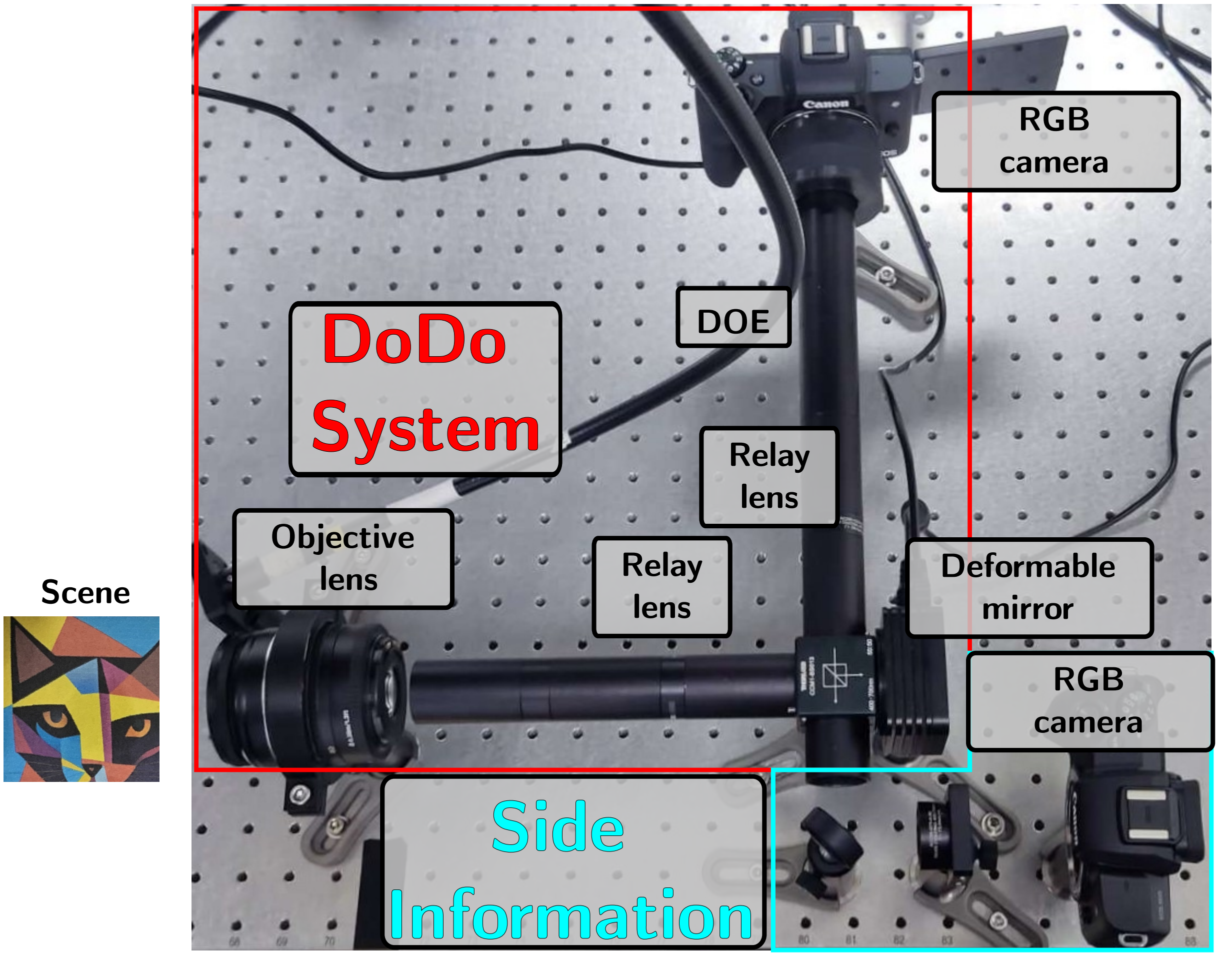

Figure 5.5. Implementation of the Double Phase Encoding system with a side information system for ground truth acquisition.

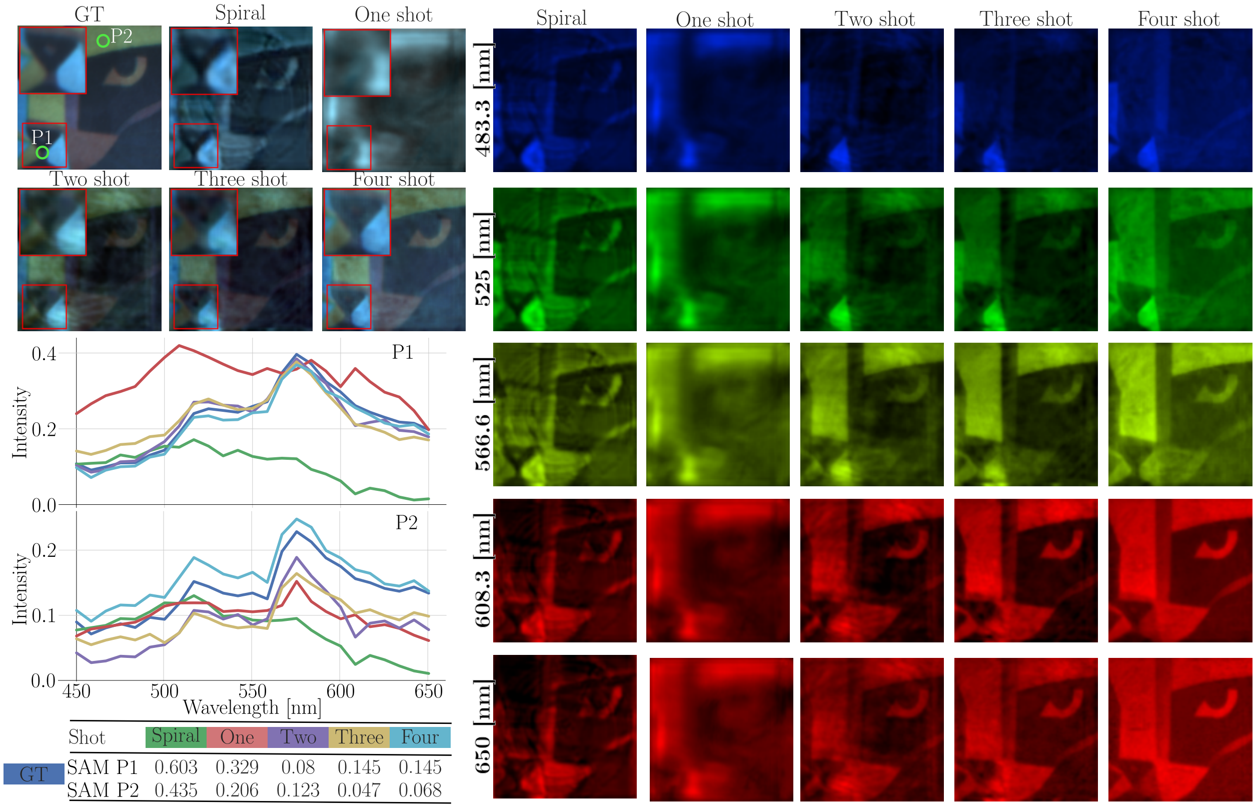

Shot	Spiral	One	Two	Three	Four
SAM P1	0.603	0.329	0.08	0.145	0.145
SAM P2	0.435	0.206	0.123	0.047	0.068

Figure 5.6. Visual results of a real captured data reconstructed employing the spiral DOE and the double DOE codification for {1,2,3,4} shots. For each reconstruction, five spectral bands are displayed and the two spectral signatures are plotted.

6. Conclusions

In this work, a differentiable mathematical model of the acquisition process of a designed compressive spectral imaging system using matrix analysis was obtained, this model of a phase-encoded compressive spectral imaging system, uses mathematical operators such as integrals, convolutions, and multiplication with complex numbers to describe the acquisition process. Also, using a proposed degradation model, a deep learning-based algorithm for alleviating the calibration distortion in an optimized compressive spectral imaging system, was developed, this model uses an end-to-end approach to optimize the phase encoding element, and a u-net was employed as a projector network to reduce the mismatch between the implemented and designed compressive spectral imaging system. To validate the proposed method, the designed compressive spectral imaging system was implemented in the laboratory of the HDSP group, this system uses 4 relay lenses, a beam splitter, a deformable mirror, and a visible camera to acquire the encoded spectral image, also using the non encoded optical path, a side information system was implemented to obtain the reference spectral image, both systems contributes to the acquisition of 12 trios composed by references spectral image, a real acquired encoded image, and a simulated acquired encoded image. These images contributed to the validation of the deep learning-based algorithm by reconstructing a spectral data cube using the enhanced measurements and were compared with the reconstruction of non-enhanced measurements.

The proposed method, through the degradation model and the correction of mismatches between simulated and laboratory-acquired scenarios, enables a significant improvement in the reconstruction quality of spectral images. Specifically, it achieves up to a 4.75 dB improvement in PSNR and a 0.07 increase in SSIM compared to traditional methods in the literature. Future work can explore new standard deviation values for the noise of the coefficients in the degradation model, as well as other types of distributions, and different compressive spectral imaging systems, to further enhance the results of the proposed method compared to traditional approaches. In addition, all the proposed specific objectives and the general objective have been fulfilled.

References

[Arad et al., 2022] Arad, B., Timofte, R., Yahel, R., Morag, N., Bernat, A., Cai, Y., Lin, J., Lin, Z., Wang, H., Zhang, Y., et al. (2022). Ntire 2022 spectral recovery challenge and data set. In *Proceedings of the IEEE/CVF Conference on Computer Vision and Pattern Recognition*, pages 863–881.

[Arce et al., 2014] Arce, G. R., Brady, D. J., Carin, L., Arguello, H., and Kittle, D. S. (2014). Compressive coded aperture spectral imaging: An introduction. *IEEE Signal Processing Magazine*, 31(1):105–115.

[Arguello and Arce, 2010] Arguello, H. and Arce, G. (2010). Code aperture design for compressive spectral imaging. In *2010 18th European Signal Processing Conference*, pages 1434–1438.

[Arguello et al., 2023] Arguello, H., Bacca, J., Kariyawasam, H., Vargas, E., Marquez, M., Hettiarachchi, R., Garcia, H., Herath, K., Haputhanthri, U., Ahluwalia, B. S., et al. (2023). Deep optical coding design in computational imaging: a data-driven framework. *IEEE Signal Processing Magazine*, 40(2):75–88.

[Arguello et al., 2021a] Arguello, H., Pinilla, S., Peng, Y., Ikoma, H., Bacca, J., and Wetzstein, G. (2021a). Shift-variant color-coded diffractive spectral imaging system. *Optica*, 8(11):1424–1434.

[Arguello et al., 2021b] Arguello, H., Pinilla, S., Peng, Y., Ikoma, H., Bacca, J., and Wetzstein, G. (2021b). Shift-variant color-coded diffractive spectral imaging system. *Optica*, 8(11):1424–1434.

[Bacca et al., 2023] Bacca, J., Martinez, E., and Arguello, H. (2023). Computational spectral imaging: a contemporary overview. *JOSA A*, 40(4):C115–C125.

[Breitenbom et al., 2017] Breitenbom, H., Naccache, R., Mazhorova, A., Clerici, M., Piccoli, R., Khorashad, L. K., Govorov, A. O., Razzari, L., Vetrone, F., and Morandotti, R. (2017). Terahertz spectral imaging and thermal sensing for biomedical applications. In *2017 42nd International Conference on Infrared, Millimeter, and Terahertz Waves (IRMMW-THz)*, pages 1–1.

[Donoho, 2006] Donoho, D. (2006). Compressed sensing. *IEEE Transactions on Information Theory*, 52(4):1289–1306.

[Figueiredo et al., 2007] Figueiredo, M. A. T., Nowak, R. D., and Wright, S. J. (2007). Gradient projection for sparse reconstruction: Application to compressed sensing and other inverse problems. *IEEE Journal of Selected Topics in Signal Processing*, 1(4):586–597.

[Fong et al., 2020] Fong, A., Shu, G., and McDonogh, B. (2020). Farm to table: Applications for new hyperspectral imaging technologies in precision agriculture, food quality and safety. In *2020 Conference on Lasers and Electro-Optics (CLEO)*, pages 1–2.

[Fornasier and Rauhut, 2015] Fornasier, M. and Rauhut, H. (2015). Compressive sensing. *Handbook of mathematical methods in imaging*, 1:187–229.

[Garcia et al., 2023] Garcia, H., Bacca, J., Wohlberg, B., and Arguello, H. (2023). Calibration reinforcement regularizations for optimized snapshot spectral imaging. *Appl. Opt.*, 62(8):C135–C145.

[Garcia et al., 2016] Garcia, H., Espitia, , and Arguello, H. (2016). Multiresolution spectral imaging by combining different sampling strategies in a compressive imager, mr-cassi. In *2016 XXI Symposium on Signal Processing, Images and Artificial Vision (STSIVA)*, pages 1–6.

[Garini et al., 2006] Garini, Y., Young, I. T., and McNamara, G. (2006). Spectral imaging: principles and applications. *Cytometry Part A: The Journal of the International Society for Analytical Cytology*, 69(8):735–747.

[Gelvez et al., 2021] Gelvez, T., Bacca, J., and Arguello, H. (2021). Interpretable deep image prior method inspired in linear mixture model for compressed spectral image recovery. In *2021 IEEE International Conference on Image Processing (ICIP)*, pages 1934–1938. IEEE.

[Huang et al., 2022] Huang, L., Luo, R., Liu, X., and Hao, X. (2022). Spectral imaging with deep learning. *Light: Science & Applications*, 11(1):61.

[Jeon et al., 2019] Jeon, D. S., Baek, S.-H., Yi, S., Fu, Q., Dun, X., Heidrich, W., and Kim, M. H. (2019). Compact snapshot hyperspectral imaging with diffracted rotation. *ACM Trans. Graph.*, 38(4).

[Kawase et al., 2011] Kawase, K., Iwasaki, A., and Shibuya, T. (2011). Terahertz spectral imaging for drug inspection. In *CLEO: 2011 - Laser Science to Photonic Applications*, pages 1–3.

[Marquez et al., 2019] Marquez, M., Rueda, H., Meza, P., Vera, E., Molina, D., and Arguello, H. (2019). Multiple snapshot colored compressive spectral imager via deformable mirrors. In *2019 XXII Symposium on Image, Signal Processing and Artificial Vision (STSIVA)*, pages 1–5.

[Mejia and Arguello, 2018] Mejia, Y. and Arguello, H. (2018). Binary codification design for compressive imaging by uniform sensing. *IEEE Transactions on Image Processing*, 27(12):5775–5786.

[Monsalve et al., 2021] Monsalve, J., Marquez, M., Esnaola, I., and Arguello, H. (2021). Compressive covariance matrix estimation from a dual-dispersive coded aperture spectral imager. In *2021 IEEE International Conference on Image Processing (ICIP)*, pages 2823–2827.

[Peng et al., 2015] Peng, Y., Fu, Q., Amata, H., Su, S., Heide, F., and Heidrich, W. (2015). Computational imaging using lightweight diffractive-refractive optics. *Opt. Express*, 23(24):31393–31407.

[Ramirez et al., 2011] Ramirez, A. B., Arguello, H., and Arce, G. (2011). Video anomaly recovery from compressed spectral imaging. In *2011 IEEE International Conference on Acoustics, Speech and Signal Processing (ICASSP)*, pages 1321–1324.

[Salazar et al., 2019] Salazar, E., Parada-Mayorga, A., and Arce, G. R. (2019). Spectral zooming and resolution limits of spatial spectral compressive spectral imagers. *IEEE Transactions on Computational Imaging*, 5(2):165–179.

[Urrea et al., 2023] Urrea, S., Jacome, R., Asif, M. S., Arguello, H., and Garcia, H. (2023). Optical solutions for spectral imaging inverse problems with a shift-variant system. In *2023 IEEE/CVF International Conference on Computer Vision Workshops (ICCVW)*, pages 4159–4166. IEEE.

[Vasudevan et al., 2017] Vasudevan, A., Anderson, A., and Gregg, D. (2017). Parallel multi channel convolution using general matrix multiplication. In *2017 IEEE 28th international conference on application-specific systems, architectures and processors (ASAP)*, pages 19–24. IEEE.

[Velasco et al., 2016] Velasco, A. C., García, C. A. V., and Fuentes, H. A. (2016). A comparative study of target detection algorithms in hyperspectral imagery applied to agricultural crops in colombia. *Revista Tecnura*, 20(49):86.

[Wang et al., 2017] Wang, Y., Reder, N., Kang, S., Glaser, A., and Liu, J. (2017). Multiplexed optical imaging of tumor-directed nanoparticles: A review of imaging systems and approaches. *Nanotheranostics*, 1:369–388.

[Wu and Arce, 2011] Wu, Y. and Arce, G. (2011). Snapshot spectral imaging via compressive random convolution. In *2011 IEEE International Conference on Acoustics, Speech and Signal Processing (ICASSP)*, pages 1465–1468.

[Yuan et al., 2021] Yuan, X., Brady, D. J., and Katsaggelos, A. K. (2021). Snapshot compressive imaging: Theory, algorithms, and applications. *IEEE Signal Processing Magazine*, 38(2):65–88.

6.1. Appendix 1: Variables table

Variable	Meaning
$\mathbf{G}$	Discrete Measurement
m	Index of row
n	Index of column
c	Channel number
x	Continuous spatial dimension in x
y	Continuous spatial dimension in y
λ	Continuous wavelength
κ_c	Wavelength sensitivity per channel
Δ	Pitch size of the sensor
$u_2(x,y)$	Encoded Wavefront
$u_0(\bar{x},\bar{y},\lambda)$	Incoming wavefront from the scene
$u_1(x'',y'')$	Propagated wavefront in the encoding element
$\mathscr{P}\{\cdot,\cdot\}$	Propagation operator
z	Propagated distance
$\phi(x'',y'',\lambda)$	Encoding operand
$h(x'',y'')$	Height map of the encoding element
Z^t	t-th Zernike Basis
β^t	Weight of the Zernike basis
N	Number of columns
M	Number of rows
$\mathbf{Y}$	Ideal measurement
$\mathscr{F}_\beta\{\mathbf{X}\}$	Ideal forward operator
$\bar{\mathbf{Y}}$	Degradated measurement
$\bar{\mathscr{F}}_\beta\{\mathbf{X}\}$	Degradated forward operator
μ_θ	Projector network
θ	Weights of the optimized network
M_ϕ	Reconstruction network of the ideal measurements
η^t	Noise coefficient for the t-th weight of the Zernike basis
β	Set of coefficients of the optimized heightmap
ϕ	Parameters of the recovery network
σ	Standard deviation of the degradation model
ε	Noise on measurements